Understanding near-infrared luminescence in Cr-doped La-gallogermanates through first-principles calculations and ligand-field theory

Longbing Shang,[1,2] Qianshan Quan,[1,2] Xiantao Wei,[1,*] and Chang-Kui Duan[1,2,3,†]

[1]*CAS Key Laboratory of Microscale Magnetic Resonance, and School of Physical Sciences, University of Science and Technology of China, Hefei 230026, China*

[2]*CAS Center for Excellence in Quantum Information and Quantum Physics, University of Science and Technology of China, Hefei 230026, China*

[3]*Hefei National Laboratory, University of Science and Technology of China, Hefei 230088, China*

(Received 31 July 2023; revised 5 October 2023; accepted 9 October 2023; published 23 October 2023)

Near-infrared phosphors based on Cr^{3+} have a wide range of important applications. The design and optimization of these phosphors require accurate determination of site occupancy and prediction of the luminescence mechanism of Cr^{3+} in solids. The former can typically be achieved through first-principles calculations of formation energies, while the latter can be accomplished through first-principles calculations aided by ligand field (LF) analyses. This study shows that it is possible to obtain all the information needed to construct adiabatic potential energy surfaces, including LF parameters and orbitals, the energies and equilibrium structures of certain states, and electron-phonon parameters, through calculation. The reliability of these results is confirmed by comparing them with experimental data. This improves the accuracy of the predictions for excitation, emission, and Stokes shift energies in the photoluminescence of Cr^{3+} ions. These calculations are then used to interpret the multipeak luminescence observed in Cr-doped La-gallogermanate systems. The results show that the Cr^{3+} ions located at a typical distorted-octahedral site in the host and another octahedral site similar to that in β–Ga_2O_3 are responsible for producing the low and high bands in the luminescence spectra of various La-gallogermanates, respectively. This study demonstrates that combining first-principles calculations with LF analysis is an effective approach for obtaining the low excited states of $3d$ transition metal activators, which has important implications for the design and optimization of luminescent materials.

DOI: 10.1103/PhysRevB.108.155136

I. BACKGROUND

Near-infrared (NIR) spectroscopy technique has wide applications in food composition and freshness analysis, night vision, and medical fields [1,2]. NIR phosphor-converted light-emitting diodes are considered as the most popular NIR light source for the low energy consumption, broad band emission and high quantum efficiency. As one of the activators in NIR phosphor of the best performance, the Cr^{3+} have the excitation peak of about 420–480 nm that benefits for the fabricating with blue LED chips, and have NIR emission peaks around 650 to 1300 nm [3] where some good performers exhibit large full width at half maximum of over 400 nm or high quantum efficiency of close to 100% [4,5].

These luminescent properties are related to the excited states of Cr^{3+} with $3d^3$ electron configuration. The Cr^{3+} in oxide tend to occupy six-coordinated site forming a regular or distorted octahedron (O_h), where the high-spin ground state is denoted as $^4A_2$ and the excited states involved in the photoluminescence include $^4T_2$, ^2E, and $^4T_1$. The energies of these excited states are determined by the Coulomb interaction between $3d$ electrons together with the LF of the O_h structure, which may be distorted. Besides, the emission process is also related to the coupling between the excited states and ionic vibration modes. Quantitative prediction of these factors is essential for the design and optimization of luminescent properties.

Several theoretical methods have been developed to describe or calculate multiplet states of transition metal (TM) ions with $3d^N$ configurations. Semiempirical LF theory combined with parameter fitting has been successfully applied to analyze experimental data on absorption and emission spectra of TM activators [6]. To predict the properties of doped TM ions, LF theory combined with Racah parameters calculated using density functional theory (DFT), known as LFDFT, the configuration interaction (CI) approach within the DFT framework (CIDFT), and time-dependent density functional theory (TDDFT) are commonly used to calculate activator excited states that account for correlation of $3d$ electrons [7,8]. These methods can reasonably predict d-d transitions in TM complexes and embedded cluster systems where the configuration states of d^n are not significantly affected by the charge transfer states. However, these methods have various limitations. For example, CIDFT tends to overestimate low-spin excited states [9], LFDFT tends to underestimate them, and TDDFT often fails to accurately describe transitions dominated by LF splitting [10]. Additionally, these methods do not provide convenient or efficient means for geometric structure

*wxt@ustc.edu.cn
†ckduan@ustc.edu.cn

optimization of excited states. The low excited states (^{2}E, ^{4}T$_2$) of Cr^{3+} activators can be approximated using single electronic configurations (t_2^3 or t_2^2e), which can be reasonably estimated using the ΔSCF method with constrained DFT (cDFT). This method is computationally efficient and capable of optimizing structures for states approximated by a single Slater determinant [11–13]. This approach will be discussed in conjunction with LF theory in the following section.

A variety of Cr^{3+} doped La (Ca,Sr)-gallogermanate systems have been investigated experimentally as NIR phosphors [14–19]. In all these experiments, two emission peaks are usually observed, a sharp R line (680–700 nm) and an ultrabroad NIR band (850–1200 nm), which are considered as from the Cr occupying two kinds of near-O_h sites with strong and weak LFs. In particular, Cr^{3+} doped $La_3Ga_5GeO_{14}$, $La_3Ga_5NbO_{14}$ and $La_3Ga_5SnO_{14}$ systems contain another broad band emission around 730–780 nm but only one near-O_h site in the host [17–19]. Such situations that more observed Cr^{3+} emission bands than the number of different O_h or near-O_h sites had led to the speculation of luminescence from Cr^{3+} occupying irregular or non-O_h sites in some works [19–21]. The first-principles calculation can be used to analyze the site occupation preference, charge state of defects, and luminescence property to discriminate different speculations, for example, we previously showed that the Cr^{3+} tetrahedral site is quenched by nonradiative process [22]. Here, a more feasible interpretation for the multiband luminescence in Cr^{3+} doped La-gallogermanate is provided with the aid of our first-principles calculation. In doing so, the combination of the ΔSCF methods in cDFT calculations and the LF analysis is proposed and examined to predict the multielectron energy-level structure of Cr^{3+} so as to predict with confidence the emission and excitation peaks of the Cr^{3+} activators in solids.

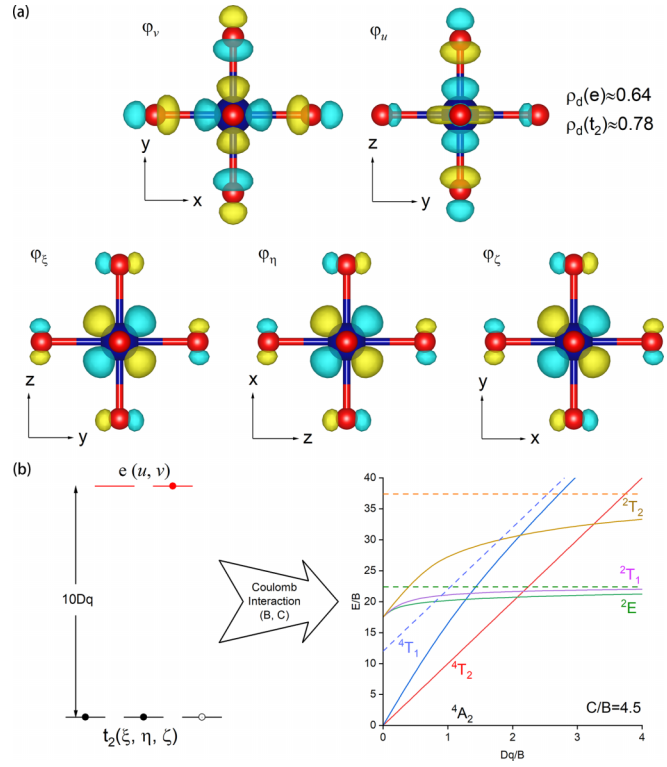

FIG. 1. (a) The wave-function isosurface of the defect Kohn-Sham orbitals in CrO_6 structure and the projected densities on the 3*d* orbitals of the transition metal are labeled. (b) The schematic diagram that the LF strength (10*Dq*) and Coulomb interaction (*B*, *C*) dominate the transition of these multiplets of TM defect. The dashed lines in the Tanabe-Sugano diagram represent the energies of the single configuration states in Eqs. (2) and (3).

II. THEORY AND CALCULATION

Before discussing the first-principles calculations, we briefly review the model of the transition metal (TM) ions multiplets, i.e., the LF theory. For TM ions with open-shell $3d^n$ electron configuration in solids, the five 3*d*-character defect orbitals are mainly composed of the TM-3*d* components with some mixing of the *p* orbitals of the ligands, as shown in Fig. 1(a). The effective $3d^n$ electronic system can be described by the following Hamiltonian [23]:

$$\hat{H}_0 = \sum_{i,j,\sigma} V_{ij}^{\mathrm{ext}}(Q) c_{i,\sigma}^{\dagger} c_{j,\sigma} + \frac{1}{2} \sum_{i,j,p,q,\sigma_1,\sigma_2} \times \left(J_{ijpq} c_{i,\sigma_1}^{\dagger} c_{j,\sigma_2}^{\dagger} c_{p,\sigma_2} c_{q,\sigma_1} + K_{ijpq} c_{i,\sigma_1}^{\dagger} c_{j,\sigma_2}^{\dagger} c_{p,\sigma_1} c_{q,\sigma_2} \right). \quad (1)$$

Here, the summations i, j, p, q and σ_1, σ_2 run over the corresponding labels of orbital and spin of the five 3*d*-character defect orbitals, $c_{i,\sigma}^{\dagger}$ and $c_{i,\sigma}$ are their corresponding creation and annihilation operators. The LF matrix elements $V_{ij}^{\mathrm{ext}}(Q)$ represent the interactions between defect orbitals and the displacements of nuclei denoted as Q, which causes the TM–3*d* orbitals to split. For the second term, the Coulomb interaction between the TM-3*d* electrons contains the direct Coulomb term J and the exchange Coulomb term K. When the defect is at O_h or T_d site, the set of parameters J and K contain only three independent parameters termed as the Racah parameters A, B, C, and the $V_{ij}^{\mathrm{ext}}(Q)$ only have one independent parameter Dq that represents the one tenth of the e–t_2 splitting as shown in Fig. 1(b). Meanwhile, the five basis orbitals can be labeled by (u, v and ξ, η, ζ) and belong to the E and T_2 representations of O_h(or T_d) group. The main 3*d* components of these defect orbitals are respectively the ($d_{z^2}, d_{x^2-y^2}, d_{yz}, d_{zx}, d_{xy}$) orbitals of TM ion as shown in Fig. 1(a), and the *d* orbital proportion of defect orbitals greatly affects the Coulomb interaction parameters. For most of systems, the symmetry of the defect LF deviates from O_h (or T_d) symmetry, which can be treated by introducing a perturbation on the interaction.

For most of the Cr^{3+} doped oxide phosphors, the LF splitting is about 1.6–2.2 eV [24], so the 3*d*–3*d* transition around visible wavelengths should only involve the transition dominated by the electron configuration t_2^3 and t_2^2e. Hence, the effective eigenstates of Eq. (1) of interest are $^4A_2$, ^2E, $^2T_1$, $^2T_2$, $^4T_2$, and $^4T_1$, where the d^3 Tanabe-Sugano (TS) diagram already lists their energy with set of parameters (Dq, B, C) as shown in Fig. 1(b). By ignoring the interactions between different electron configurations, i.e., under the strong LF limit, these multiplets can be expressed approximately as the following single configuration states, which are the eigenstates of the O_h LF and Coulomb interaction within single electron configurations. Some degenerate states with different orbital

and spin magnetic are not listed here, such as $|^2\mathrm{E}, v, m_s = \frac{1}{2}\rangle$ and $|^4\mathrm{A}_2, m_s = \frac{1}{2}\rangle$, which can be obtained in this book [23].

(1) Configuration t_2^3:

$$\begin{aligned}
\left|^4\mathrm{A}_2, m_s = \frac{3}{2}\right\rangle &= |\xi^\uparrow \eta^\uparrow \zeta^\uparrow|;\\
\left|^2\mathrm{E}, u, m_s = \frac{1}{2}\right\rangle &= \frac{1}{\sqrt{2}}(|\xi^\uparrow \eta^\downarrow \zeta^\uparrow| - |\xi^\downarrow \eta^\uparrow \zeta^\uparrow|);\\
\left|^2\mathrm{T}_1, \alpha, m_s = \frac{1}{2}\right\rangle &= \frac{1}{\sqrt{2}}(|\xi^\uparrow \zeta^\uparrow \zeta^\downarrow| - |\xi^\downarrow \eta^\uparrow \eta^\downarrow|);\\
\left|^2\mathrm{T}_2, \xi, m_s = \frac{1}{2}\right\rangle &= \frac{1}{\sqrt{2}}(|\xi^\uparrow \zeta^\uparrow \zeta^\downarrow| + |\xi^\downarrow \eta^\uparrow \eta^\downarrow|). \qquad (2)
\end{aligned}$$

(2) Configuration $t_2^2 e$:

$$\begin{aligned}
\left|^4\mathrm{T}_2, \zeta, m_s = \frac{3}{2}\right\rangle &= |\xi^\uparrow \eta^\uparrow v^\uparrow|;\\
\left|^4\mathrm{T}_2, \xi, m_s = \frac{3}{2}\right\rangle &= \left|\eta^\uparrow \zeta^\uparrow\left(-\frac{1}{2}v^\uparrow - \frac{\sqrt{3}}{2}u^\uparrow\right)\right|;\\
\left|^4\mathrm{T}_2, \eta, m_s = \frac{3}{2}\right\rangle &= \left|\zeta^\uparrow \xi^\uparrow\left(-\frac{1}{2}v^\uparrow + \frac{\sqrt{3}}{2}u^\uparrow\right)\right|;\\
\left|^4\mathrm{T}_1, \gamma, m_s = \frac{3}{2}\right\rangle &= |\xi^\uparrow \eta^\uparrow u^\uparrow|;\\
\left|^4\mathrm{T}_1, \alpha, m_s = \frac{3}{2}\right\rangle &= \left|\eta^\uparrow \zeta^\uparrow\left(-\frac{1}{2}u^\uparrow + \frac{\sqrt{3}}{2}v^\uparrow\right)\right|;\\
\left|^4\mathrm{T}_1, \beta, m_s = \frac{3}{2}\right\rangle &= \left|\zeta^\uparrow \xi^\uparrow\left(-\frac{1}{2}u^\uparrow - \frac{\sqrt{3}}{2}v^\uparrow\right)\right|. \qquad (3)
\end{aligned}$$

The energies of the states $^4\mathrm{A}_2$, $^2\mathrm{E}$, $^2\mathrm{T}_1$, $^2\mathrm{T}_2$, $^4\mathrm{T}_2$, and $^4\mathrm{T}_1$ are 0, $3C + 9B$, $3C + 9B$, $5C + 15B$, $10Dq$, and $10Dq + 12B$. These are represented as dashed lines in the TS diagram, as shown in Fig. 1(b). The eigenstates $^4\mathrm{A}_2$ and $^4\mathrm{T}_2$ of Eq. (1) are single Slater states without showing configuration interaction, and the eigenstates $^2\mathrm{E}$, $^2\mathrm{T}_1$ are close enough to the green dashed line represented by $^2\mathrm{E}$ in Eq. (2). The Racah parameters describing the 3d–3d Coulomb interaction should be roughly independent of the ionic configuration Q. The Racah parameters and the Q-dependent ligand-field together determine the configuration coordinate diagram containing the ground the some of the lowest excited states, which will be determined via first-principles calculations in the following to analyze the excited-state relaxation processes.

In addition, the radiative relaxation of the excited states can vary significantly across different systems. This is because the electric dipole transition, which is initially forbidden due to factors such as parity, spin, or more general point group selection rules, can be enabled by various weaker interactions (more discussion in Ref. [25], see also [26,27] therein). Calculating transition rates with precision using first-principle methods is a demanding task and is not the focus of this study. However, as a general guideline, the radiative decay rates of the spin-forbidden and spin-allowed transitions for Cr^{3+} are the order of 10–100 s^{-1} and about 3 orders of magnitude faster, respectively. These rates may decrease further if the system possesses space inversion symmetry.

We performed the calculations by employing the VASP code [28], which expands the wavefunction with the projected augment wave method [29]. The corresponding recommended pseudopotentials of the atoms were adopted. The single Γ k point was chosen for the supercell calculation. The Perdew-Burke-Ernzerhof functional revised for solids (PBEsol) [30] exchange correlation functional was employed and 520 eV cutoff energy is used. The DFT+U [31] and the Heyd-Scuseria-Ernzerhof hybrid (HSE06) functional [32] were used to correct the localization of $3d$ orbitals. Specially, a damped velocity friction algorithm with switching off the subspace diagonalization was adopted for the convergence of the iteration, which conserves the initial set orbital order when ΔSCF method with HSE06 functional was used for the static calculations of the excited state. All structural optimization calculations were performed with DFT+U method with subspace diagonalization switched on. Small U close to zero were used for the convergence of the ΔSCF calculations (more details on the DFT calculations and supercell sizes can be founded in Ref. [25]).

A. Average occupation method for $V_{ij}^{\mathrm{ext}}(Q)$

Assuming that Racah parameters are known and do not vary with the multiplets, the excited state energies can be estimated with the model of Eq. (1) as long as the LF parameter $V_{ij}^{\mathrm{ext}}(Q)$ is obtained. Restricting the occupation numbers of defect Khon-Sham (KS) orbitals to be equal in the SCF calculation with cDFT can be used to obtain the $V_{ij}^{\mathrm{ext}}(Q)$, and the similar strategy is used in LFDFT calculation to determine the basis function of the LF model [33]. In DFT calculations, the KS orbitals are the eigenstates of the following KS equation:

$$\left(-\frac{\nabla^2}{2} + V^{\mathrm{ext}}(r) + \int dr' \frac{n_\uparrow(r') + n_\downarrow(r')}{|r - r'|} + \frac{\delta E^{\mathrm{xc}}[n_\uparrow(r) + n_\downarrow(r)]}{\delta n_\sigma(r)}\right)\phi_{i,\sigma}(r) = \lambda_{i,\sigma}\phi_{i,\sigma}(r); \qquad (4)$$

$$n_\sigma(r) = \sum_i f_{i,\sigma}|\phi_{i,\sigma}(r)|^2. \qquad (5)$$

Here $n_\sigma(r)$ represents the total electron density with spin σ and $f_{i,\sigma}$ is the occupation number of KS orbital $\phi_{i,\sigma}$. In the cDFT calculation of this work, a constraint on $f_{i,\sigma}$ is set in the iteration of solving KS equation, where the usual set for the ground state of insulator is that $f_{i,\sigma}$ is 1 for $\lambda_{i,\sigma}$ lower than the Fermi level and zero otherwise. The sum of $f_{i,\sigma}$ equals the total number of electrons in the calculated systems. Certain unusual settings can be used for some on-purpose designed DFT calculations, such as the Slater transition state method for calculating the excitation energy [34], the core electron binding energies calculations [35] and the spin-purified ΔSCF calculations on excitation energies [36]. For the five local defect orbitals of TM defect, the kinetic energy term, the potential energy term and the exchange correlation energy term in Eq. (4) will be equal if the total electron density $n_\uparrow(r) + n_\downarrow(r)$ is spherically symmetric for the TM ion center. Therefore, $\lambda_{i,\sigma}$ of the five defect orbitals will only depend on

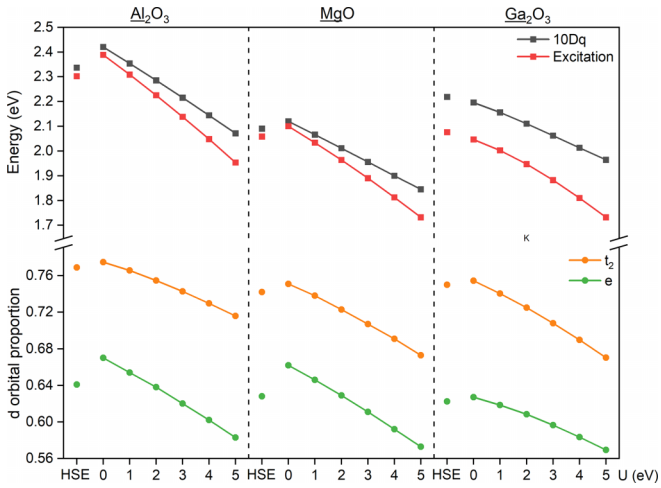

FIG. 2. The relation between the Dq parameter, $^4T_2$ excitation energy and the (t_2, e) orbital projection on the TM ion d orbitals of the Cr^{3+} doped Al_2O_3, MgO and β–Ga_2O_3 and the GGA+U and hybrid functional in the DFT calculations.

the external potential term and the $V_{ij}^{\text{ext}}(Q)$ can be obtained according to these eigenvalues and eigenstates of Eq. (4) ($\boldsymbol{V}^{\text{ext}} = \boldsymbol{M}^{\text{T}}\boldsymbol{\lambda}\boldsymbol{M}$, where $\boldsymbol{M}$ is the transfer matrix between eigenstates and basis). However, it is difficult to obtain the perfect spherical defect electron density by restricting the occupation numbers, such as making $f_{i,\uparrow} = 0.6$ and $f_{i,\downarrow} = 0$, as the five KS orbitals shown in Fig. 1(a) are not pure $3d$ orbitals but have varying proportions. Therefore, many parameters that describe the exchange-correlation functional will influence the calculated $V_{ij}^{\text{ext}}(Q)$.

As shown in Fig. 2, the larger U parameter will lead to less-pure $3d$ LF orbitals, i.e., smaller $\sum_i |\langle d_i||\zeta\rangle|^2$, and decreased LF strength ($10Dq \approx \lambda_{\text{e}}^{\text{ave}} - \lambda_{\text{t}_2}^{\text{ave}}$). The calculated $3d$ orbital proportion, $10Dq$ and excitation energies with HSE06 functional are close to the those with $U \approx 0$ eV. It can be interpreted as that the V^{ext} is only weakly dependent on the exchange-correlation functional and the splitting of defect KS orbitals is almost constant as long as the KS orbitals are similarly described. The excitation energy is dominated by the strength of LF and has similar tendency with the $10Dq$. The $10Dq$ minus $^4T_2$ excitation energy of $Ga_2O_3 : Cr^{3+}$ is larger than those of $Al_2O_3 : Cr^{3+}$ and $MgO : Cr^{3+}$ because the former has larger $^4T_2$ splitting due to the LF distortion and the calculated excitation energy corresponds to the lowest $^4T_2$ sublevel. In the following transition energy calculations, the HSE06 functional is used instead of DFT+U, as it can provide a better description of the band gap and the interaction between localized $3d$ orbitals and band states, and the Coulomb interaction is shown to be better described by taking the experiments as reference.

B. ΔSCF method for Coulomb interaction

The ΔSCF method in the following cDFT calculations means optimizing a hypothetical electronic density with constrained $f_{i,\sigma}$ to approximate the excited state, and the energy difference between the two calculated states represents the transition energy. The SCF solution of the KS equation, where all $f_{i,\sigma}$ are either 1 or 0, approximately represents a many-electronic state $|\phi_{1,\sigma_1}\cdots\phi_{N,\sigma_N}|$, which is a Slater determinant of N occupied KS orbitals. For the Cr^{3+} defect, that single Slater determinant can be simplified to $|\{\phi_{1,\sigma_1}, \phi_{2,\sigma_2}, \phi_{3,\sigma_3}\}|$ that consists three occupied local $3d$ orbitals with mixing from host band orbitals. To describe the single configuration state in Eqs. (2) and (3), these single Slater states $|\xi^\uparrow\eta^\uparrow v^\uparrow|$, $|\xi^\uparrow\eta^\uparrow u^\uparrow|$, $|\xi^\uparrow\eta^\uparrow\zeta^\downarrow|$, and $|\xi^\uparrow\zeta^\uparrow\zeta^\downarrow|$ should be calculated, with their energies described by $10Dq$, $10Dq + 12B$, $2C + 6B$, $4C + 12B$ with appropriate effective parameters.

During the ΔSCF calculations of these single Slater states, the $f_{i,\sigma}$ settings are illustrated in Fig. 3(a), which shows the states of Cr^{3+} replacing Mg in MgO as an example, along with the KS orbitals and their energies obtained via cDFT calculation. The energy of an occupied KS orbital is much lower than that of its unoccupied counterpart in DFT+U and HSE06 functionals, but they are nearly equal in the PBEsol functional. This difference is due to a significant change in self-interaction when an orbital changes from being occupied to being empty in DFT+U and HSE06 calculations, which is not the case in PBEsol. This effect can be problematic when solving the constrained KS equation using SCF, so a damped algorithm that turns off subspace diagonalization to maintain the constrained orbital order is used to avoid this issue. The energies of these single Slater states are still influenced by the parameters in E_{xc}, as shown in Figs. 3(b) and 3(c), where larger U values result in larger calculated Racah parameters (B, C). The energies of the single Slater states were calculated using Racah parameters ($B \approx 82$ meV, $C \approx 390$ meV) obtained by fitting experimental data [3] and are represented by dashed lines in Figs. 3(b) and 3(c). The calculated value of $3C + 9B$ ($1.5E(|\xi^\uparrow\eta^\uparrow\zeta^\downarrow|)$) using the HSE06 functional is underestimated by approximately 5%, as shown by the red dashed line in Fig. 3(b), and can provide an estimate of the ^2E energy, which is also approximately 5% lower than the actual value of $3C + 9B$, as shown by the TS diagram in Fig. 1(b). To further verify the ΔSCF calculation of B, the energies of four single Slater states labeled in Fig. 3(c) were calculated. It can be seen that the ratio of excited state energies relative to $|\xi^\uparrow\eta^\uparrow v^\uparrow|$ is close to 1:3:4, corresponding to the parameters $3B$, $9B$, and $12B$. The calculated energy of $|\xi^\uparrow\eta^\uparrow v^\uparrow|$ is much lower than the experimentally fitted value because the ΔSCF calculation includes d-ligand interaction, which reduces the calculated effective value of B. In summary, ΔSCF calculations provide estimates of single Slater state energies for occupied KS orbitals and perform well for low excited states, aiding analysis of Coulomb interaction in $d-d$ transitions. Additionally, the HSE06 hybrid functional performs well for estimation and is used for subsequent ΔSCF calculations.

C. Calibration of the predictions via experimental data

The experimental concerned emission of Cr^{3+} is dominated by the $^2E \rightarrow {}^4A_2$ or $^4T_2 \rightarrow {}^4A_2$ transitions. It is necessary to analyze the error of the average occupation and ΔSCF method relative to the experiments in order to verify the prediction ability. The energy $E(^2E)$ (relative to the ground state) is estimated via $1.5[E(|\xi^\uparrow\eta^\uparrow\zeta^\downarrow|) - E(^4A_2)]$, while both methods, total energy difference and ligand-field splitting of orbitals, are adopted to estimated the energy of

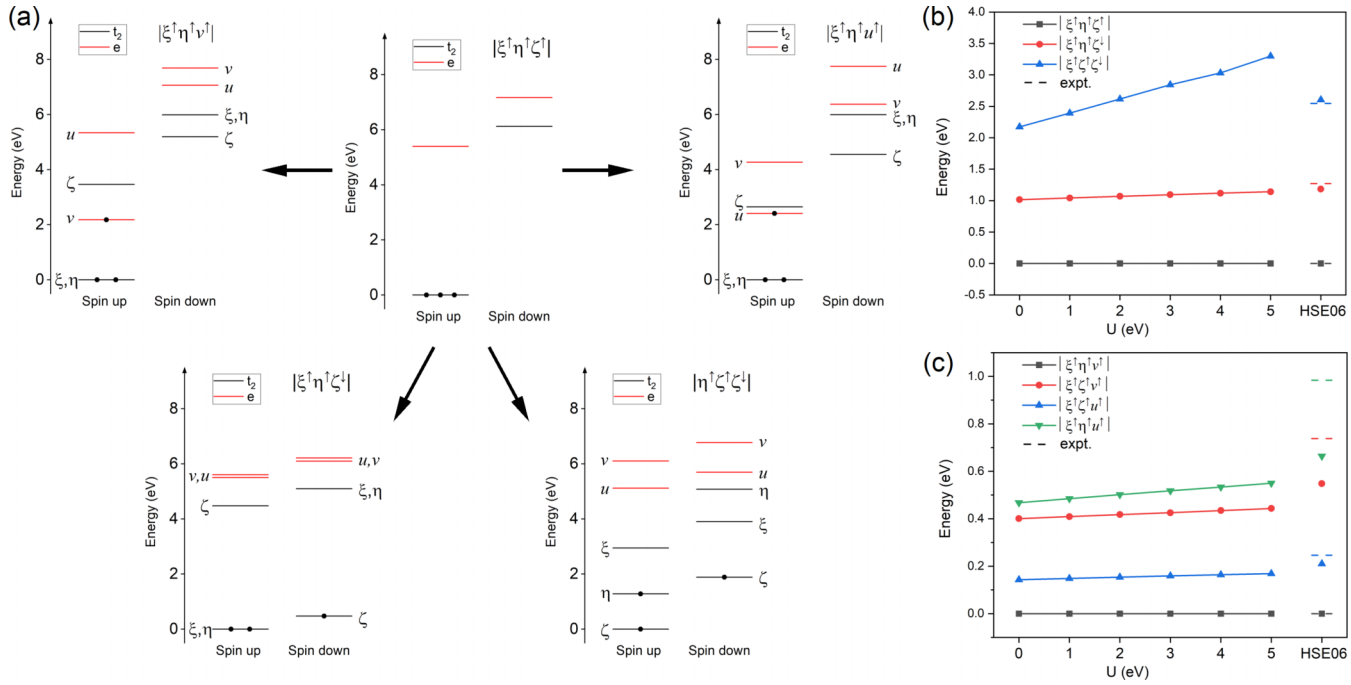

FIG. 3. (a) The energy splitting of the ten KS orbitals in ΔSCF calculation, where lines with dots represent occupied orbitals, and the five occupations correspond to the five single Slater states $|\xi^{\uparrow}\eta^{\uparrow}v^{\uparrow}|$, $|\xi^{\uparrow}\eta^{\uparrow}\zeta^{\uparrow}|$, $|\xi^{\uparrow}\eta^{\uparrow}u^{\uparrow}|$, $|\xi^{\uparrow}\eta^{\downarrow}\zeta^{\uparrow}|$ and $|\xi^{\uparrow}\zeta^{\uparrow}\zeta^{\downarrow}|$. (b) and (c) show the relation between the energies of single Slater states and the density functional, where their energies repressed by parameters are respectively (0, $2C + 6B$ and $4C + 12B$) and ($10Dq$, $10Dq + 3B$, $10Dq + 9B$ and $10Dq + 12B$), where the corresponding values obtained by B and C derived from experimental energies by fitting are plotted by dashed lines. The result shows that the Coulomb interaction in SCF calculations is weakly dependent on the density functional.

$E(^4T_2)$ (relative to the ground state) for comparison. In the average occupation method, the eigenstates and eigenvalues of the LF are obtained. The $|\xi^{\uparrow}\eta^{\uparrow}\zeta^{\uparrow}| \rightarrow |\xi^{\uparrow}\eta^{\uparrow}v^{\uparrow}|$ transition energy equals to $\lambda_v - \lambda_\zeta$, which can be directly estimated by $\lambda_4 - \lambda_3$. Here, λ_i is the ith eigenvalue with ascending order in the average occupation calculation. The $\lambda_4 - \lambda_3$ may be smaller than $\lambda_v - \lambda_\zeta$ when the two eigenstates deviate from v and ζ. The λ_v and λ_ζ can be obtained from λ_i by the transformation between the basis orbitals (u, v, ξ, η, ζ) and the eigenstates, but there is an error due to the artificial choice on the principal axis of the basis orbitals, and the accuracy is not improved much.

Taking the lowest $^4T_2$ excitation and emission peak in Cr^{3+} doped Al_2O_3, Al_2SiO_5, MgO, $MgWO_4$, Sc_2O_3, $LiScGeO_4$, $LiInSiO_4$, Ga_2O_3, Ga_4GeO_8, and $Y_3Ga_5O_{12}$ observed in experiments as references, the corresponding energies calculated by the average occupation and ΔSCF methods with HSE06 functional are shown in Figs. 4(a)–4(d). The ΔSCF method can give a better estimate than the average occupation method, where the dashed lines are fitted linearly by the black points without loops and the dotted lines represent adding the residual standard error (RSE). The results show that there is an overestimation at the high energy end and an underestimation at the low energy end. The encircled points 3 and 7b represent the Cr^{3+} replacing Mg in MgO and replacing Li in $LiInSiO_4$, whose calculated emission peaks are far from the dashed line due to their small Stokes shift. Besides, the compound defects with charge compensation, $Cr_{Mg} + Vac_{Mg}$ and $Cr_{Li} + Li_{In}$ represented correspondingly by points 3c and 7c, have a lager Stokes shift and are more close to the dashed line. Previous work also has mentioned this view on the compound defects luminescence [40]. The ^2E energy and $^4T_2$ Stokes shift can also be predicted well by ΔSCF method as shown in Figs. 4(e) and 4(f). The blue points represent the comparison of the Cr doped La-gallogermanate systems and are consistent with the prediction of dashed line [14,17–19,48].

In summary, the ΔSCF method with the HSE06 functional can accurately predict the $^4T_2$ and ^2E energies of Cr^{3+}, provided that convergence of the SCF calculation iteration is carefully managed. The fitting lines $y = 1.778 + 0.856(x - 1.778) \pm 0.043$ and $y = 1.497 + 0.863(x - 1.497) \pm 0.058$ (in units of eV) can be used to calibrate the $^4T_2$ excitation and emission peak. In these equations, x and y represent calculated and predicted values, respectively, and the uncertainty is the RSE of the linear regression $\{\sum_{i=1}^{n}[y(x_i) - y_{exp}(x_i)]^2/(n - p - 1)\}^{1/2}$, where $n = 11$ and $p = 2$ are the number of data points and parameters, respectively. The average occupation method can provide the eigenvalues and eigenstates of the LF at nucleus configuration Q, which can be used to directly estimate $^4T_2$ energies. This method does not have convergence problems during iteration, but has a larger calculation error than the ΔSCF method.

D. ΔSCF method for excited state structures

In ΔSCF calculations, the equilibrium structures of the excited states can be directly obtained by optimizing initial structure with constraining the electronic states, approximately as a statistic result of electron-phonon coupling.

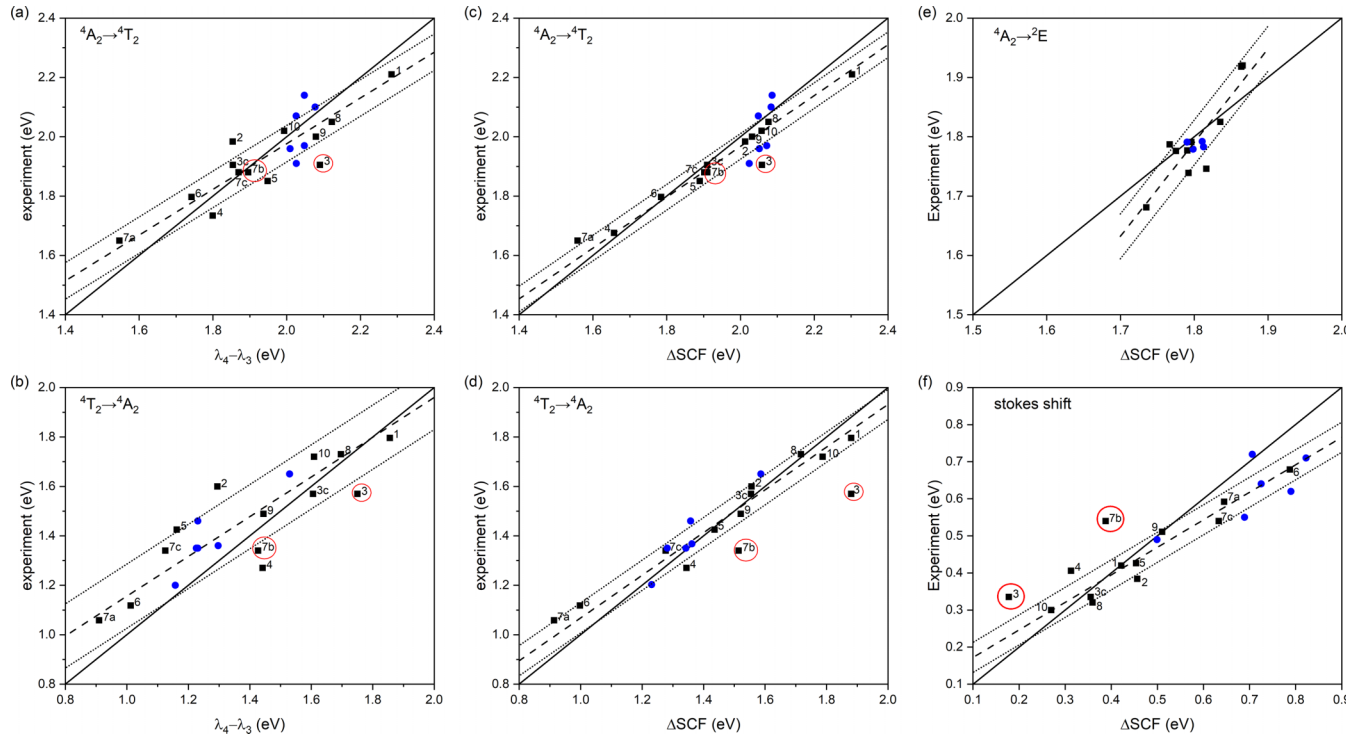

FIG. 4. Diagrams to calibrate calculation results with experimental data. The excitation ($^4A_2 \rightarrow {}^4T_2$) and emission ($^4T_2 \rightarrow {}^4A_2$) energies calculated with the average occupation method and ΔSCF method are shown in (a), (b) and (c), (d), respectively. The comparisons between calculations and experiments of sharp R lines ($^4A_2 \rightarrow {}^2E$) and the Stokes shift of $^4T_2$ states are shown in (e) and (f). The blue points represent the Cr doped La-gallogermanate systems which will be discussed in Section III, and the black points 1–10 represent Cr^{3+} doped Al_2O_3 [37,38], Al_2SiO_5 [39], MgO [40], $MgWO_4$ [41], Sc_2O_3 [42], $LiScGeO_4$ [43], $LiInSiO_4$ [44], Ga_2O_3 [45],Ga_4GeO_8 [46], and $Y_3Ga_5O_{12}$ [47], where the dashed lines are fitted by the black points without loops and dotted lines represent adding the residual standard error on them.

Taking the equilibrium structure of ground state as the reference, the excited state structures can be the result of the linear coupling between the local vibration modes Q_k and defect orbitals as a good estimation for the CrO_6 defect with small Stokes shift by the following equation (omitting spin for simplicity):

$$\hat{H}_p + \hat{H}_{ep} = \sum_k \left(\frac{1}{2}\hat{P}_k^2 + \frac{\omega_k^2}{2} Q_k^2 \right) + \sum_{i,j,k} K_{ijk} c_i^\dagger c_j Q_k. \quad (6)$$

In the frame of CrO_6 with O_h point group symmetry, the main Q_k projected to the nearest O atoms include $Q(A_{1g})$, $Q(E_g)$ and $Q(T_{2g})$ as shown in Eq. (A1) of Appendix, and there are five independent coupling parameters K_{ijk} for these modes as shown in Eq. (A2). There parameters can be calculated by the averaged occupied method as the $\partial_{Q_k} V_{ij}^{\text{ext}}(Q_0) = K_{ijk}$ shown in Eq. (1). Taking the MgO:Cr^{3+} as an example, these parameters are obtained by adding the corresponding displacement of modes in Eq. (A1) on the O_h symmetric CrO_6 as shown in Figs. 5(a)–5(c), where the calculated points in the region $|Q| < 0.1$ are used to fit the parameters. The A_{1g} and E_g modes that change bond length have larger K than the T_{2g} that change bond angle. The inverse anti-symmetric modes $Q(T_{1u})$ and $Q(T_{2u})$ are not discussed here because these modes lack linear coupling with the electronic state with parity, and the coupling parameters K_{ijk} are close to zero for systems with the ground state structures of approximately space inversion.

As indicated by the matrix elements in Eq. (A2), the modes A_{1g} and E_g are blocked-diagonal, with each ($t_2^n e^m$) configuration forming a block, as the coefficients of $c_e^\dagger c_{t_2}$ for these two modes are zero. Consequently, the excited states $^4T_2$ have the coupling parameters of the A_{1g} and E_g modes as K_1 and $K_2 - 2K_3$, respectively. As for the T_{2g} modes, the coupling cannot be fully described in the ΔSCF calculation due to nonzero $c_e^\dagger c_{t_2}$ elements in Eq. (A2). However, this has only a minimal impact, as the first-order perturbation contribution of the T_{2g} modes to the coupling strength vanishes, while those of the second-order contributions, which are proportional to $K_5^2/3(K_2 - 2K_3)$ and K_4^2/Dq, turn out to be small and can be neglected. Therefore, the main modes that should be considered in the coupling model in Eq. (6) are A_{1g} and E_g, which can be obtained in the total energy calculations. It is meaningful to analyze the potential surface of the excited state $^4T_2$. After the $^4A_2 \rightarrow {}^4T_2$ excitation, the nonradiative transition between three sublevels of $^4T_2$ excited states is dominated only by the coupling with E_g modes because these sublevels have the same $Q(A_{1g})$. As shown in Fig. 5(d), the potential surfaces of the three sublevels are distorted paraboloids and their envelope surface is close to a pleated Mexican hat. This schematic result shows the coupling between E_g modes and the $^4T_2 \oplus {}^4T_1$ states where the model parameters are listed in the next paragraph. The actual saddle point of the pleated Mexican hat will be lower than the modeled one due to the additional Jahn-Taller effect, and is usually smaller than 0.1 eV relative to the minimum for the Cr^{3+} doped oxides.

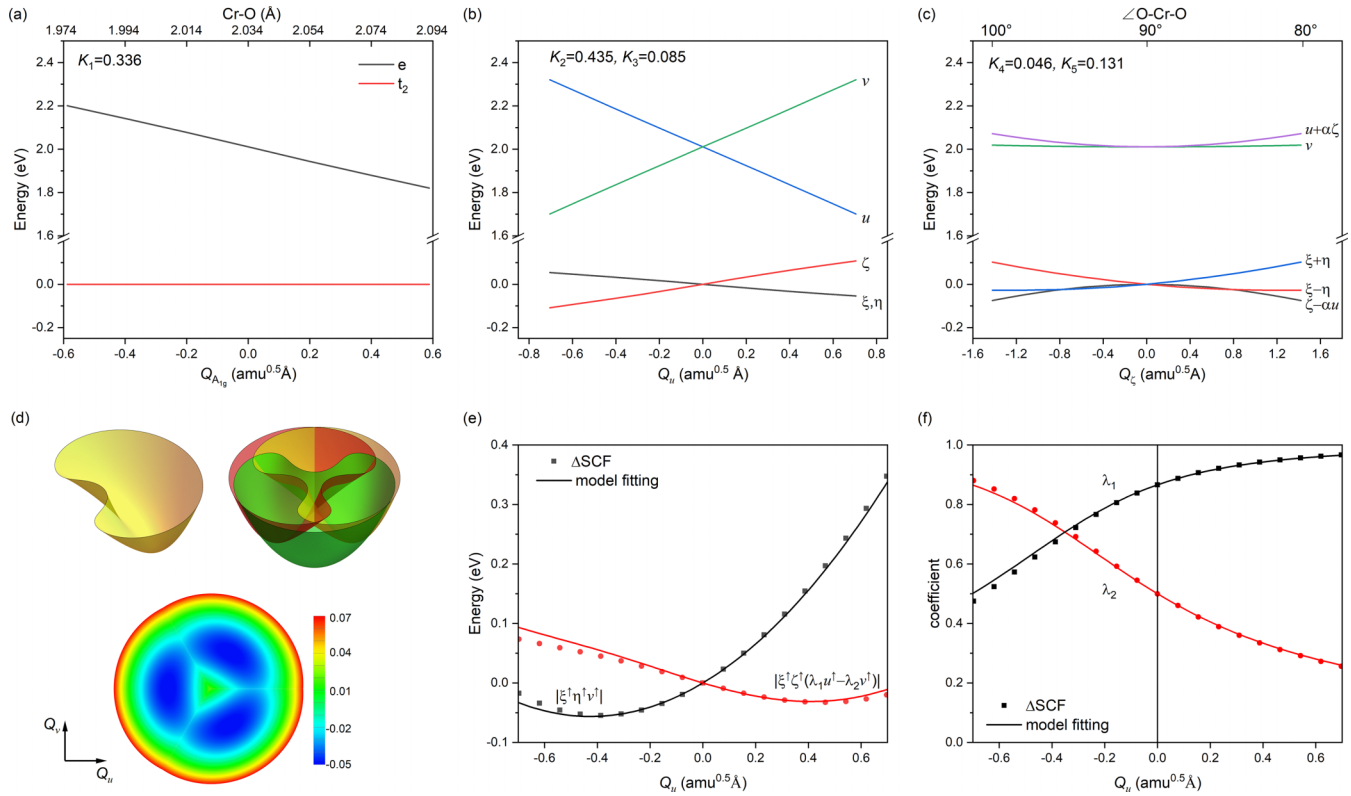

FIG. 5. Splitting of the localized orbitals (a–c) and multiplet states (e,f) of the dopant along canonical vibration coordinates of modes $Q(\mathrm{A_{1g}})$, $Q(\mathrm{E}_g)$ and $Q(\mathrm{T_{2g}})$ given as abscissa. The coupling parameters K_1–K_5 as described in Eq. (6) are given in (a)–(c), (e), and (f). The coupling between $Q(\mathrm{E}_g)$ modes and excited states $^4\mathrm{T}_2$ and $^4\mathrm{T}_1$ is included in the simulation. The energies of eigenstates $|\xi^\uparrow\eta^\uparrow v^\uparrow|$ and $|\xi^\uparrow\zeta^\uparrow(\lambda_1 u^\uparrow - \lambda_2 v^\uparrow)|$ in ΔSCF calculation and parameter fitting are compared in (e), where the parameters are $B = 50.9$ meV, $K_2 = 0.435$, and $K_3 = 0.085$ in units of eV/($\sqrt{\text{amu}}$ Å), and $Q(\mathrm{E}_g)$ phonon energy is 50 meV. The coefficient of state $|\xi^\uparrow\zeta^\uparrow(\lambda_1 u^\uparrow - \lambda_2 v^\uparrow)|$ is compared in (f).

The distorted CrO_6 has a tilted $^4T_2$ potential surface and the saddle point will disappear when the distortion is large enough (such as t_2 splitting is larger than 0.15 eV).

To further illustrate the coupling between single Slater excited states and vibration modes using the ΔSCF method, a comparison between the coupling model presented in the Appendix for $\mathrm{E}_g \otimes (^4\mathrm{T}_2 \oplus {}^4\mathrm{T}_1)$ and corresponding results from first-principles calculations is shown in Figs. 5(e) and 5(f). The model parameters in Eq. (A4) were chosen as $B = 50.9$ meV, $K_2 = 0.435$, and $K_3 = 0.085$ in units of eV/(amu$^{0.5}$Å), based on previous calculations, and the E_g phonon energy was fitted as 50 meV to match the calculated value of $E(|\xi^\uparrow\eta^\uparrow\zeta^\uparrow|) - E(Q(\mathrm{O_h})]$. The high-symmetry structure $Q(\mathrm{O_h})$ in the calculation was obtained by optimizing with constrained occupations (for each orbital, $n_{t_2} = 2/3$ and $n_e = 1/2$). The structures calculated along the $Q(\mathrm{O_h})$–$Q(|\xi^\uparrow\eta^\uparrow\zeta^\uparrow|)$ path were dominated by displacement of the E_g modes with a weight of 98%. The successful fit indicates that the ΔSCF method is capable of accurately describing the coupling between vibration modes and single Slater states, and that the structure can be reliably determined. Furthermore, implementation with first-principles calculations of the coupling model between defect electrons and local vibration modes, as well as its application in first-principles calculations, can be utilized to analyze excited state potential surfaces and optical transition profiles in future studies.

III. THE LUMINESCENCE OF Cr^{3+} DOPED $A_3BC_2D_3O_{14}$ SYSTEMS

The La-gallogermanate (space group P321, No. 150) family is usually solid solution and has four kinds of cation sites (AO_8, BO_6, CO_4, DO_{4-6}) that form the $A_3BC_2D_3O_{14}$ formula as shown in Fig. 6. In this work, the Cr^{3+} doped systems $La_3Ga(Ga/Ge)Ga_3O_{14}$, $La_3(Nb_{1/2}/Ga_{1/2})Ga_2Ga_3O_{14}$, $La_3SnGa_2Ga_3O_{14}$, $La_3Ga(Ga/Si)Ga_3O_{14}$, and $(Na_2/Ca)GeGe_2Ge_3O_{14}$ are studied, where the elements in parentheses share the same cation site to form a solid solution. They have a sharp R line emission around 680–700 nm and a broad emission with its peak around 850–1200 nm (low), which are generally considered as the $^2\mathrm{E} \rightarrow {}^4\mathrm{A}_2$ and $^4\mathrm{T}_2 \rightarrow {}^4\mathrm{A}_2$ transitions, respectively. In the first three systems, another broad band emission with its peak around 730–780 nm (high) has been observed coexisting with the two above-mentioned emissions. Its excitation spectrum also has the characteristic of Cr^{3+} in O_h LF, leading to its interpretation as Cr^{3+} occupying another near-O_h site in previous works. This will be explored using the first-principles calculations. These solid solution structures are represented by the lowest energy structure within the 92 atoms supercell in calculations.

The case of Cr^{3+} replacing the B site of BO_6 in the host is considered first. The excitation and emission energies of

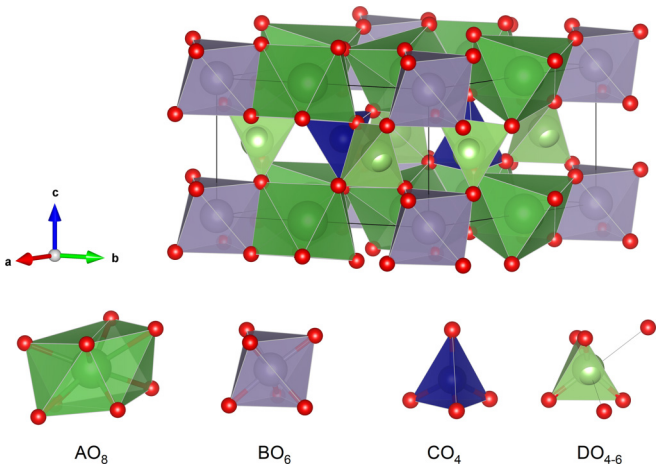

FIG. 6. Primitive cell structure of La-gallogermanate solid solution starting with the space group *P*321. There are four kinds of cation sites AO_8, BO_6, CO_4, and DO_{4-6}, where the D site has four small and two long D–O bonds. The ratio of these sites can be expressed in the formula $A_3BC_2D_3O_{14}$.

$^4T_2$, and the zero-phonon line energies of $^4T_2$ and ^2E were calculated by the ΔSCF method and the results are listed in Table I. The atoms substituted by Cr^{3+} are underlined. The comparison between the calculated $^4T_2$ excitation and emission energies with these in experiments are shown as the blue points in Fig. 4, and the errors mostly within one RSE imply that the Cr^{3+} on BO_6 site with a large Stokes shift (0.75 eV in calculations) is the activator for the low energy broad emission of the five systems. In Cr^{3+} doped $(Na_2/Ca)GeGe_2Ge_3O_{14}$ and $La_3Ga(Ga/Si)Ga_3O_{14}$, the coexistent emission of R line and low energy broad band can be interpreted by that the sites with large Stokes shift have similar $^4T_2$ and ^2E ZPLs (1.79 eV) as shown in Table I. Meanwhile, the higher intensity ratio of the R line in $(Na_2/Ca)GeGe_2Ge_3O_{14}$ than in $La_3Ga(Ga/Si)Ga_3O_{14}$ [14,48] can be interpreted by the fact that the former has a higher $^4T_2$ ZPL, as shown in Table I, and so the higher occupation ratio of the ^2E state at the Boltzmann thermal equilibrium of the ^2E versus $^4T_2$ distribution.

More elaborately, the ground state structure Q_0 of CrO_6 has the symmetry of D_3 point group, and the t_2 orbitals split into two single electron levels $a_1(t_2)$ and $e(t_2)$ separated by ∼0.1 eV, while the *e* orbitals remain degenerate. The excited state equilibrium structures (Q_ξ, Q_η, Q_ζ) should have the same energies as they permute under D_3 operation. The structure change $Q_0 \rightarrow Q_\zeta$ is dominated by the E_g and A_{1g} modes, and the Cr off-center modes are shown by the arrows in Fig. 7(b). The off-center mode appears in the excited state structure for the systems without the inverse symmetry and contribute 15% to the structure relaxation energy $E(Q_0)$–$E(Q_\zeta)$. The corresponding pleated Mexican hat surface as discussed in Sec. II D has almost no tilt, with the $E(Q_0)$–$E(Q_\zeta) \approx 0.27$ eV and the saddle point of the surface calculated by the nudged elastic band method [49] being less than 0.1 eV above the minimum. The elaborate results show that there is no new meta-stable point on the $^4T_2$ energy surface to produce a new emission band. In brief, CrO_6 at the BO_6 site is common in La-gallogermanate and produces the lower energy broad emission in all the five systems, and the coexistent emission of the sharp line in $(Na_2/Ca)GeGe_2Ge_3O_{14}$ and $La_3Ga(Ga/Si)Ga_3O_{14}$ systems is attributed to the emission from ^2E states of this site. The high-energy broad emissions in the other three systems will be discussed below.

Firstly, we discuss the possible roles played by other cation sites in luminescence despite their low substitution concentration relative to BO_6, for example, the Cr^{3+} replacing the

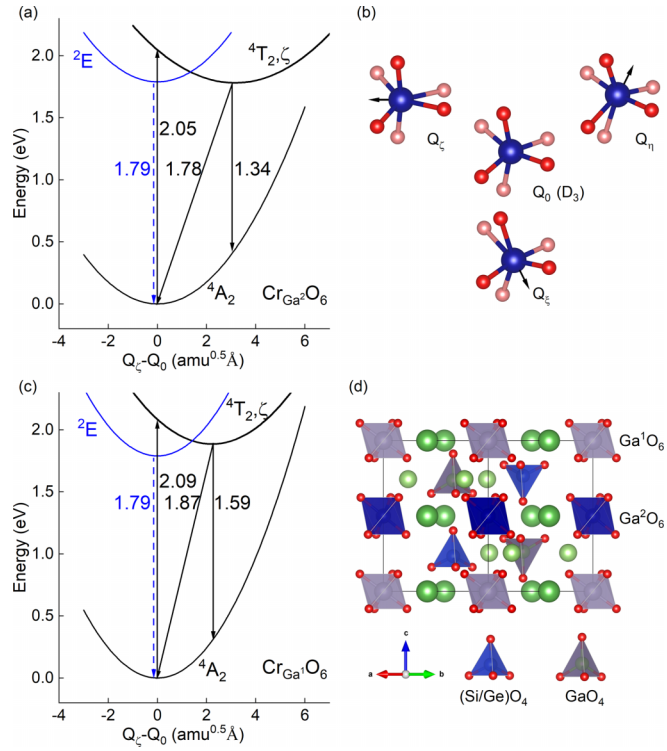

FIG. 7. The configuration coordinate diagrams of Cr^{3+} occupying the Ga^2O_6 and Ga^1O_6 sites in $La_3Ga(Ga/Ge)Ga_3O_{14}$ are shown in (a) and (c), respectively. The two sites belong to BO_6 and their surrounding atoms are shown in (d), which is a chosen structure of the solid solution with Ga/Ge or Ga/Si CO_4-site solution. Only the energy curves of sublevel ζ of $^4T_2$ are shown in (a) and (c), the other two sublevels have almost the same curves due to the D_3 point group nature of the ground structures, and their equilibrium configurations are shown in (b) where the arrows represent the off-center displacements.

TABLE I. The calculated excitation, emission, zero-phonon-line (ZPL) energies of $^4T_2$ and the ZPL energies (in units of eV) of ^2E of Cr^{3+} activators calculated via the ΔSCF method. The sites in the hosts substituted by Cr^{3+} are underlined. We note that an error of a few 0.01 eV should be allowed when applying those results to interpret experimental results.

system	exc.	emis.	$^4T_2^{ZPL}$	$^2E^{ZPL}$
$La_3\underline{Ga}(Ga/Ge)Ga_3O_{14}$	2.058	1.343	1.782	1.790
$La_3(Nb/\underline{Ga})_{1/2}Ga_2Ga_3O_{14}$	2.024	1.231	1.728	1.791
$La_3\underline{Sn}Ga_2Ga_3O_{14}$	2.051	1.362	1.791	1.813
$La_3\underline{Ga}(Ga/Si)Ga_3O_{14}$	2.072	1.292	1.771	1.798
$(Na_2/Ca)\underline{Ge}Ge_2Ge_3O_{14}$	2.083	1.358	1.845	1.811

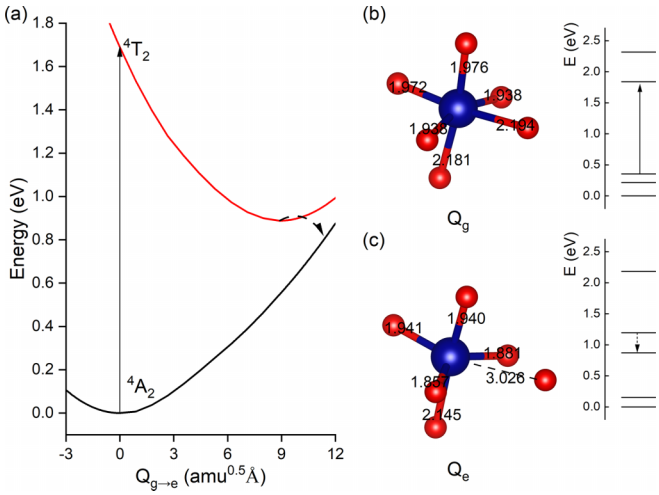

FIG. 8. The configuration coordinate diagram of Cr^3+ occupying GaO_{4-6} site in $La_3Ga(Ga/Ge)Ga_3O_{14}$ is shown in (a), where the excited activator goes through a large structure relaxation and then decays nonradiatively to the ground state. At the ground state configuration Q_g, the structure is close to O_h site and the excitation is also close to the $^4A_2 \to {}^4T_2$ where the splitting of the defect orbitals is large as shown in (b). For the excited state configuration Q_e, the Cr ion has five close O atoms and the defect orbitals splitting is shown in (c), which is close to the A + E + E result of C_3 point group, and the ground state and excited state cannot be labeled by $^4A_2$ and $^4T_2$.

AO_8, CO_4, and DO_{4-6} sites in $La_3Ga(Ga/Ge)Ga_3O_{14}$ have formation energies about 3.5, 1.8 and 0.6 eV higher than that of BO_6 site. For the CO_4 site, the tetrahedral $Cr^{4+}O_4$ site usually has an emission peak around 1200–1600 nm [50], while $Cr^{3+}O_4$ does not emit, but relaxes to the ground state nonradiatively via the connection of vibration potential surfaces due to the Jahn-Taller distortion [22]. Second, for the DO_{4-6} site with four short C–O bonds (∼1.85 Å) and two long C–O bonds (∼2.71 Å), the Cr^{3+} occupancy leads to shortening the two long bonds to 2.18 Å and forming an irregular O_h site for Cr^{3+}, as illustrated by Fig. 8(b). However, as shown in Fig. 8(a), the structure relaxation energy of the excited state is so large that the excitation will relax to the ground state nonradiatively. This can be interpreted as the much smaller energy $\hbar\omega$ of the dominant vibration mode than the near-O_h site. The excited state equilibrium structure is close to CrO_5, since one of the oxygen atoms brought close by the ground state of Cr^{3+} dopant moves away due to excited-state relaxation. This result appears to be general because if the ground state of Cr^{3+} on the site changes much on the bond length due to some vibration mode, then the same vibration mode can be relaxed to release the change in bond length once that the electron involving in that bond is excited, leading to a large Stokes shift. Therefore, the potential assignment of some NIR emission to the DO_{4-6} site in La-gallogermanate is ruled out [20], so is in the case of the Cr-doped $CaAl_4O_7$ [21]. Lastly, Cr^{3+} on AO_8 sites, besides being unlikely to form due to its much high formation energy, do not have the favorable LF splitting to produce NIR luminescence. Above all, no NIR emission is from the other direct cation site.

The broad emission with peak around 730–780 nm observed in Cr^{3+} doped $La_3Ga(Ga/Ge)Ga_3O_{14}$, $La_3(Nb/Ga)_{1/2}Ga_2Ga_3O_{14}$, and $La_3SnGa_2Ga_3O_{14}$ systems cannot be attributed to direct site occupation in the host materials and requires further interpretation. In experiments, this emission disappears at low temperatures, leaving only a sharp R line, indicating the presence of a type of $Cr^{3+}O_6$ with a $^4T_2$ ZPL higher than the ^2E ZPL and a small Stokes shift (∼0.4 eV) for $^4T_2$. In the $La_3Ga(Ga/Ge)Ga_3O_{14}$ systems, there are two near-O_h sites, Ga^1O_6 and Ga^2O_6, when the solid solution sites CO_4 are distributed as shown in Fig. 7(d). Cr^{3+} occupying the Ga^1O_6 site has a smaller Stokes shift than that of Ga^2O_6, and the ZPL of the broad band is higher than that of the ^2E, as shown in Fig. 7(c). These two substitutions of Cr^{3+} have nearly identical formation energies (differing by only 15 meV) and ^2E energies, suggesting their probable coexistence and potentially explaining the two broad emissions and R line. A similar situation exists in the $La_3Ga(Ga/Si)Ga_3O_{14}$ systems, but Cr^{3+} occupying the Ga^1O_6 site has a much higher $^4T_2$ ZPL (1.95 eV) than its ^2E, meaning that the high-energy broad emission cannot be observed at low or even room temperature, consistent with experimental observations [14]. However, this conjecture is invalid for the $La_3(Nb_{1/2}/Ga_{1/2})Ga_2Ga_3O_{14}$ and $La_3SnGa_2Ga_3O_{14}$ hosts because the solid solution site BO_6 is far away from the substituted site and the pure phase does not have a near-O_h site that produces a small Stokes shift. Such a site would need to resemble the GaO_6 site in β–Ga_2O_3, which also exhibits temperature-dependent broad emission around 730–760 nm and has a similar excitation spectrum to that of the high-energy broad emission [51]. Additionally, calculation results labeled as point 8 in Fig. 4 are consistent with this assignment. Therefore, we propose that a local structure resembling GaO_6 in Ga_2O_3 could be formed during synthesis of La-gallogermanate or left over from raw ingredients. This proposition explains the observed high-energy emission band. Similar emissions observed in Cr^{3+} and Mn^{4+} doped $CaAl_4O_7$, where no normal near-O_h site exists, are similar to those observed in $CaAl_{12}O_{19}$ [52] and can also be explained by this proposition. Briefly, the high-energy broad emissions in these three systems originate from a site very close to a regular O_h that produces a small Stokes shift, closely resembling that in β–Ga_2O_3. This site is either formed due to random distribution of CO_4 structure or other minor phases formed or left over during synthesis processes.

IV. CONCLUSIONS

In conclusion, this study examined the use of first-principles calculations combined with LF analysis to investigate the luminescence of Cr^{3+} ions. The average occupation method with the HSE06 hybrid functional was found to be effective in estimating LF parameters of defect structures without convergence problems in constrained DFT calculations. The ΔSCF method was employed to calculate the energy of single Slater states, which were used to analyze Racah parameters and estimate the energy of low excited states. Additionally, the structure of the excited state $^4T_2$, which is dominated by coupling with the E_g and A_{1g} vibration modes, was accurately obtained using the ΔSCF method. Calibration lines derived by comparing calculated and experimental

data demonstrated the quantitative predictability of the ΔSCF calculation for excitation, emission energies, and Stokes shift of the $^4T_2$ and ^2E excited states of the Cr^{3+} activator.

These calculations were then applied to interpret the multipeak luminescence of Cr-doped La-gallogermanate systems ($A_3BC_2D_3O_{14}$), which are often solid solutions and have many potential cation sites for Cr ions to occupy. The results showed that the ultrabroad NIR emission around 850–1200 nm in all La-gallogermanates originates from Cr^{3+} substituting the usual BO_6 site, which has a large Stokes shift of 0.6–0.8 eV. Coexistent R line emissions from the ^2E state in $Na_2CaGe_6O_{14}$ and $La_3Ga_5SiO_{14}$ were also attributed to this site. Analysis of the CO_4 and AO_8 sites indicated that no observed emission was possible due to unfavorable formation energy and nonradiative relaxation of the excited state of Cr^{3+} at tetrahedral sites. The results for the atypical DO_{4-6} site showed that although introducing a Cr^{3+} ion could change the effective ligand number by bringing two ligand O^{2-} ions closer, no emission from such sites was possible due to nonradiative relaxation all the way down to the ground state bridged by structural relaxation. The sharp R line and broad band emission with peak around 730–780 nm for $La_3Ga_5GeO_{14}$, $La_3Ga_5NbO_{14}$, and $La_3Ga_5SnO_{14}$ were attributed to a near-O_h site with a Stokes shift of only approximately 0.4 eV. This type of site is not formed directly and has two different origins: (1) modification of the BO_6 site by random distribution at CO_4 by Ga/Ge as a result of solid solution, such as in $La_3Ga_5GeO_{14}$; or (2) formation or residual presence during synthesis due to a site with similar temperature-dependent emission and excitation spectra as Cr^{3+} occupying a near-O_h site in β–Ga_2O_3. Overall, these results demonstrate that ΔSCF calculations with constrained occupation provide reliable analysis of LF and luminescence properties for low excited states of Cr^{3+}, and offer a detailed interpretation for multiband luminescence in Cr-doped La-gallogermanate systems. These calculations can also be adapted to analyze other 3*d* transition metal ions in solids.

ACKNOWLEDGMENTS

We acknowledge the support of Innovation Program for Quantum Science and Technology (Grants No. 2021ZD0302200 and No. 2021ZD0303204), the National Natural Science Foundation of China (Grants No. 62375255 and No. 11974338), the Anhui Initiative in Quantum Information Technologies (Grant No. AHY050000), and the National Key Research and Development Program of China (Grant No. 2018YFA0306600). The numerical calculations were performed on the supercomputing system at the Supercomputing Center of the University of Science and Technology of China. We used VASPKIT [53] and VESTA [54] to display our results.

APPENDIX

The local vibration modes A_{1g}, E_g, and T_{2g} in Eq. (6) projected on the defect structure CrO_6 can be expressed as the following equations:

$$\begin{aligned}
Q(A_{1g}) &= \frac{\sqrt{m}}{\sqrt{6}}[(Z_1 - Z_4) + (X_2 - X_5) + (Y_3 - Y_6)];\\
Q(E_g, u) &= \frac{\sqrt{m}}{2\sqrt{3}}[2(Z_1 - Z_4) - (X_2 - X_5) - (Y_3 - Y_6)];\\
Q(E_g, v) &= \frac{\sqrt{m}}{2}[(X_2 - X_5) - (Y_3 - Y_6)];\\
Q(T_{2g}, \xi) &= \frac{\sqrt{m}}{2}[(Z_3 - Z_6) + (Y_1 - Y_4)];\\
Q(T_{2g}, \eta) &= \frac{\sqrt{m}}{2}[(X_1 - X_4) + (Z_2 - Z_5)];\\
Q(T_{2g}, \zeta) &= \frac{\sqrt{m}}{2}[(Y_2 - Y_5) + (X_3 - X_6)].
\end{aligned} \tag{A1}$$

Here, X_i represents the displacement of O_i ($i = 1$–6) ligand along the X direction, and the atoms O_1 and O_4, O_2 and O_5, O_3 and O_6 are respectively positioned along the Z, X, and Y direction, and m represents the mass of O atom.

The electron-phonon coupling Hamiltonian of the A_{1g}, E_g, and T_{2g} modes in Eq. (6) can be expressed as the following equation [55], where the basis functions are (u, v, ξ, η, ζ) and only the excited states involved in the $d-d$ transition are considered.

$$\hat{H}_{ep}^{A_{1g}} = \begin{pmatrix} -\frac{3}{5} & 0 & 0 & 0 & 0\\ 0 & -\frac{3}{5} & 0 & 0 & 0\\ 0 & 0 & \frac{2}{5} & 0 & 0\\ 0 & 0 & 0 & \frac{2}{5} & 0\\ 0 & 0 & 0 & 0 & \frac{2}{5} \end{pmatrix} K_1 Q; \quad \hat{H}_{ep}^{E_g} = \begin{pmatrix} -K_2Q_u & K_2Q_v & 0 & 0 & 0\\ K_2Q_v & K_2Q_u & 0 & 0 & 0\\ 0 & 0 & -K_3(Q_u - \sqrt{3}Q_v) & 0 & 0\\ 0 & 0 & 0 & -K_3(Q_u + \sqrt{3}Q_v) & 0\\ 0 & 0 & 0 & 0 & 2K_3Q_u \end{pmatrix};$$

$$\hat{H}_{ep}^{T_{2g}} = \begin{pmatrix} 0 & 0 & -K_4Q_\xi & -K_4Q_\eta & 2K_4Q_\zeta\\ 0 & 0 & \sqrt{3}K_4Q_\xi & -\sqrt{3}K_4Q_\eta & 0\\ -K_4Q_\xi & \sqrt{3}K_4Q_\xi & 0 & K_5Q_\zeta & K_5Q_\eta\\ -K_4Q_\eta & -\sqrt{3}K_4Q_\eta & K_5Q_\zeta & 0 & K_5Q_\xi\\ 2K_4Q_\zeta & 0 & K_5Q_\eta & K_5Q_\xi & 0 \end{pmatrix}. \tag{A2}$$

where the matrix element at i row and j column represents the term $\sum_k K_{ijk} c_i^\dagger c_j Q_k$ for k in A_{1g}, E_g and T_{2g} modes.

The Coulomb interaction between $^4T_2$ and $^4T_1$ in O_h LF can be expressed as the following matrix.

$$3B\begin{pmatrix} 1 & 0 & 0 & \sqrt{3} & 0 & 0 \\ 0 & 1 & 0 & 0 & -\sqrt{3} & 0 \\ 0 & 0 & 4 & 0 & 0 & 0 \\ \sqrt{3} & 0 & 0 & 3 & 0 & 0 \\ 0 & -\sqrt{3} & 0 & 0 & 3 & 0 \\ 0 & 0 & 0 & 0 & 0 & 0 \end{pmatrix}, \tag{A3}$$

where B is the Racah parameter and the basis functions are $|\eta^\uparrow\zeta^\uparrow u^\uparrow|$, $|\zeta^\uparrow\xi^\uparrow u^\uparrow|$, $|\xi^\uparrow\eta^\uparrow u^\uparrow|$, $|\eta^\uparrow\zeta^\uparrow v^\uparrow|$, $|\zeta^\uparrow\xi^\uparrow v^\uparrow|$, and $|\xi^\uparrow\eta^\uparrow v^\uparrow|$. Considering the Coulomb interaction between $^4T_2$ and $^4T_1$ and their static electron-phonon coupling with E_g mode, the $^4T_2$ solution of $E_g \otimes (^4T_2 \oplus {}^4T_1)$ coupling in model $\hat{H}_0 + \hat{H}_p + \hat{H}_{ep}$, as shown by Eqs. (1) and (6), can be expressed as follows:

$$\begin{aligned} E\left(^4T_2, \zeta\right) &= \frac{\omega^2}{2}\left(Q_u^2 + Q_v^2\right) - 2K_3Q_u + 6B \\ &\quad - \sqrt{K_2^2\left(Q_u^2 + Q_v^2\right) - 12BK_2Q_u + 36B^2}; \\ E\left(^4T_2, \eta/\xi\right) &= \frac{\omega^2}{2}\left(Q_u^2 + Q_v^2\right) + K_3Q_u \pm \sqrt{3}K_3Q_v + 6B \\ &\quad - \sqrt{K_2^2\left(Q_u^2 + Q_v^2\right) + 6BK_2Q_u \pm 6\sqrt{3}K_2Q_v + 36B^2}. \end{aligned} \tag{A4}$$

where B, K_2, and K_3 are Racah and coupling parameters, and ω is the frequency of vibration mode E_g.

[1] G. Liu and Z. Xia, Modulation of thermally stable photoluminescence in Cr^{3+}-based near-infrared phosphors, J. Phys. Chem. Lett. **13**, 5001 (2022).

[2] J. Qiao, G. Zhou, Y. Zhou, Q. Zhang, and Z. Xia, Divalent europium-doped near-infrared-emitting phosphor for light-emitting diodes, Nat. Commun. **10**, 5267 (2019).

[3] S. Adachi, Review-photoluminescence properties of Cr^{3+}-activated oxide phosphors, ECS J. Solid State Sci. Technol. **10**, 026001 (2021).

[4] S. Miao, Y. Liang, D. Chen, R. Shi, X. Shan, Y. Zhang, F. Xie, and X.-J. Wang, Site-Selective Occupancy control of Cr ions toward ultrabroad-band infrared luminescence with a spectral width up to 419 nm, ACS Appl. Mater. Interfaces **14**, 53101 (2022).

[5] E. T. Basore, W. Xiao, X. Liu, J. Wu, and J. Qiu, Broadband near-infrared garnet phosphors with near-unity internal quantum efficiency, Adv. Opt. Mater. **8**, 2000296 (2020).

[6] S. Adachi, New analysis model for the determination of racah and crystal-field splitting parameters: Verification and case studies, ECS J. Solid State Sci. Technol. **9**, 046004 (2020).

[7] S. Ghosh, P. Verma, C. J. Cramer, L. Gagliardi, and D. G. Truhlar, Combining wave function methods with density functional theory for excited states, Chem. Rev. **118**, 7249 (2018).

[8] M. Atanasov, P. Comba, C. A. Daul, and F. Neese, The Ligand-Field Paradigm, in *Models, Mysteries and Magic of Molecules*, edited by Jan C.A. Boeyens and J. F. Ogilvie (Springer, Netherlands, Dordrecht, 2008), pp. 411–445.

[9] M. Atanasov, E.-L. Andreici Eftimie, N. M. Avram, M. G. Brik, and F. Neese, First-principles study of optical absorption energies, ligand field and spin-hamiltonian parameters of Cr^{3+} ions in emeralds, Inorg. Chem. **61**, 178 (2022).

[10] F. Vlahović, M. Perić, M. Gruden-Pavlović, and M. Zlatar, Assessment of TD-DFT and LF-DFT for study of *d–d* transitions in first row transition metal hexaaqua complexes, J. Chem. Phys. **142**, 214111 (2015).

[11] P. Ramos and M. Pavanello, Low-lying excited states by constrained DFT, J. Chem. Phys. **148**, 144103 (2018).

[12] D. Strubbe, Density-functional perturbation theory for excited states from constrained DFT, in *APS March Meeting Abstracts*, APS Meeting Abstracts, Vol. 2018 (2018), p. A29.011.

[13] Q. Chen, L. Shang, H. Xu, C. Ma, P. A. Tanner, and C.-K. Duan, Rationalizing the structural changes and spectra of manganese and their temperature dependence in a series of garnets with first-principles calculations, Phys. Rev. B **105**, 035158 (2022).

[14] M. Casalboni, A. Luci, U. M. Grassano, B. V. Mill, and A. A. Kaminskii, Optical spectroscopy of $La_3Ga_5SiO_{14}$:Cr^{3+} crystals, Phys. Rev. B **49**, 3781 (1994).

[15] P. I. Macfarlane, T. P. J. Han, B. Henderson, and A. A. Kaminskii, Cr^{3+} Luminescence in calcium and strontium gallogermanate, Opt. Mater. (Amsterdam) **3**, 15 (1994).

[16] B. Sun, P. Dai, H. Zhu, and M. Zhang, Site-Selective Occupation of Cr^{3+} ions toward ultra-broadband near-infrared emission stannate phosphors, Mater. Today Chem. **26**, 101258 (2022).

[17] V. Rajendran, M.-H. Fang, G. N. De Guzman, T. Lesniewski, S. Mahlik, M. Grinberg, G. Leniec, S. M. Kaczmarek, Y.-S. Lin, K.-M. Lu *et al.*, Super broadband near-infrared phosphors with high radiant flux as future light sources for spectroscopy applications, ACS Energy Lett. **3**, 2679 (2018).

[18] Y. Li, S. Ye, and Q. Zhang, Ultra-broadband Near-Infrared luminescence of ordered–disordered multi-sited Cr^{3+} in $La_3Ga_{5.5}Nb_{0.5}O_{14}$:$Cr^{3+}$, J. Mater. Chem. C **2**, 4636 (2014).

[19] Y. Shi, Z. Wang, J. Peng, Y. Wang, S. He, J. Li, R. Li, G. Wei, Y. Yang, and P. Li, Achieving the ultra-broadband near-infrared $La_3SnGa_5O_{14}$:Cr^{3+} phosphor via multiple lattice sites

occupation for biological nondestructive detection and night-vision technology, Mater. Today Adv. **16**, 100305 (2022).

[20] G. N. A. De Guzman, V. Rajendran, Z. Bao, M.-H. Fang, W.-K. Pang, S. Mahlik, T. Lesniewski, M. Grinberg, M. S. Molokeev, G. Leniec, S. M. Kaczmarek, J. Ueda, K.-M. Lu, S.-F. Hu, H. Chang, and R.-S. Liu, Multi-Site cation control of ultra-broadband near-infrared phosphors for application in light-emitting diodes, Inorg. Chem. **59**, 15101 (2020).

[21] L. Vasylechko, V. Stadnik, V. Hreb, Y. Zhydachevskyy, A. Luchechko, V. Mykhaylyk, H. Kraus, and A. Suchocki, Synthesis, Crystal structure and photoluminescent properties of red-emitting $CaAl_4O_7 : Cr^{3+}$ nanocrystalline phosphor, Inorganics **11**, 205 (2023).

[22] L. Shang, M. Liu, and C.-K. Duan, Does Cr^{3+} occupy tetrahedral sites and luminesce in oxides? A first-principles exploration, J. Phys. Chem. Lett. **13**, 10635 (2022).

[23] S. Sugano, *Multiplets of Transition-Metal Ions in Crystals* (Elsevier, 2012).

[24] P. Dang, Y. Wei, D. Liu, G. Li, and J. Lin, Recent advances in chromium-doped near-infrared luminescent materials: Fundamentals, optimization strategies, and applications, Adv. Opt. Mater. **11**, 2201739 (2023).

[25] See Supplemental Materials at http://link.aps.org/supplemental/10.1103/PhysRevB.108.155136 for the discussion on the transition selection rules of the transition metal dopant, and the details of the calculation method and the supercell size of the calculated materials, which includes additional Refs. [26,27].

[26] M. H. Nazaré, J. C. Lopes, and A. J. Neves, Nickel related defects in diamond: the 2.51eV band, Phys. B: Condens. Matter **308-310**, 616 (2001).

[27] S. Sugano, A. L. Schawlow, and F. Varsanyi, Zeeman effect of the purely cubic field fluorescence line of $MgO:Cr^{3+}$ crystals, Phys. Rev. **120**, 2045 (1960).

[28] G. Kresse and J. Hafner, *Ab initio* molecular dynamics for liquid metals, Phys. Rev. B **47**, 558 (1993).

[29] P. E. Blöchl, Projector augmented-wave method, Phys. Rev. B **50**, 17953 (1994).

[30] G. I. Csonka, J. P. Perdew, A. Ruzsinszky, P. H. T. Philipsen, S. Lebègue, J. Paier, O. A. Vydrov, and J. G. Ángyán, Assessing the performance of recent density functionals for bulk solids, Phys. Rev. B **79**, 155107 (2009).

[31] S. L. Dudarev, G. A. Botton, S. Y. Savrasov, C. J. Humphreys, and A. P. Sutton, Electron-energy-loss spectra and the structural stability of nickel oxide: An LSDA+U study, Phys. Rev. B **57**, 1505 (1998).

[32] A. V. Krukau, O. A. Vydrov, A. F. Izmaylov, and G. E. Scuseria, Influence of the exchange screening parameter on the performance of screened hybrid functionals, J. Chem. Phys. **125**, 224106 (2006).

[33] M. Atanasov, C. A. Daul, and C. Rauzy, New insights into the effects of covalency on the ligand field parameters: A DFT study, Chem. Phys. Lett. **367**, 737 (2003).

[34] S. R. Billeter and D. Egli, Calculation of nonadiabatic couplings with restricted open-shell kohn-sham density-functional theory, J. Chem. Phys. **125**, 224103 (2006).

[35] N. A. Besley, A. T. B. Gilbert, and P. M. W. Gill, Self-consistent-field calculations of core excited states, J. Chem. Phys. **130**, 124308 (2009).

[36] T. Kowalczyk, S. R. Yost, and T. V. Voorhis, Assessment of the ΔSCF density functional theory approach for electronic excitations in organic dyes, J. Chem. Phys. **134**, 054128 (2011).

[37] G. Salek, A. Devoti, E. Lataste, A. Demourgues, A. Garcia, V. Jubera, and M. Gaudon, Optical properties versus temperature of Cr-Doped γ-and α-Al2O3: Irreversible Thermal Sensors Application, J. Lumin. **179**, 189 (2016).

[38] W. H. Fonger and C. W. Struck, Temperature dependences of Cr^{+3} radiative and nonradiative transitions in ruby and emerald, Phys. Rev. B **11**, 3251 (1975).

[39] M. Gaft, W. Strek, L. Nagli, G. Panczer, G. R. Rossman, and L. Marciniak, Laser-induced time-resolved luminescence of natural sillimanite Al_2SiO_5 and synthetic Al_2SiO_5 activated by chromium, J. Lumin. **132**, 2855 (2012).

[40] M. O. Henry, J. P. Larkin, and G. F. Imbusch, Nature of the broadband luminescence center in $MgO:Cr^{3+}$, Phys. Rev. B **13**, 1893 (1976).

[41] L. Zhang, Y. Huang, S. Sun, F. Yuan, Z. Lin, and G. Wang, Thermal and spectral characterization of Cr^{3+}:$MgWO_{4-a}$ promising tunable laser material, J. Lumin. **169**, 161 (2016).

[42] S. Kück, L. Fornasiero, E. Mix, and G. Huber, Spectroscopic properties of Cr-doped Sc_2O_3, J. Lumin. **87-89**, 1122 (2000).

[43] Z. Ye, Z. Wang, Q. Wu, X. Huo, H. Yang, Y. Wang, D. Wang, J. Zhao, H. Suo, and P. Li, A single luminescence center ultra-broadband Near-Infrared $LiScGeO_4$:Cr Phosphor for biological tissue penetration, Dalton Trans. **50**, 10092 (2021).

[44] Y. Zhuang, J. Luo, Y. Teng, S. Ye, B. Zhu, and J. Qiu, Broadband infrared luminescence of Cr^{3+}-doped $LiInSiO_4$ phosphors, J. Mater. Res. **25**, 224 (2010).

[45] Y. Tokida and S. Adachi, Photoluminescence spectroscopy and energy-level analysis of metal-organic-deposited $Ga_2O_3:Cr^{3+}$ films, J. Appl. Phys. **112**, 063522 (2012).

[46] L. Yao, Q. Shao, M. Shi, T. Shang, Y. Dong, C. Liang, J. He, and J. Jiang, Efficient ultra-broadband $Ga_4GeO_8:Cr^{3+}$ phosphors with tunable peak wavelengths from 835 to 980 nm for NIR pc-LED Application, Adv. Opt. Mater. **10**, 2102229 (2022).

[47] H. Yang, W. Zhao, X. Lin, Z. Liao, Z. Nie, L. Luo, W. Zhang, Z. Hu, and J. Zhong, Hundreds of times of photo-stimulation with low energy light as a new reused bio-imaging phosphor from Cr^{3+}, Si^{4+}-doped $Y_3Ga_5O_{12}$, J. Lumin. **219**, 116871 (2020).

[48] S. Ding, P. Feng, J. Cao, X. Ma, and Y. Wang, Multiple coordination of chromium ion luminescence: A strategy for designing ultra-broadband nir long persistent luminescent materials, ACS Appl. Mater. Interfaces **14**, 44622 (2022).

[49] G. A. Henkelman, B. P. Uberuaga, and H. Jónsson, A climbing image nudged elastic band method for finding saddle points and minimum energy paths, J. Chem. Phys. **113**, 9901 (2000).

[50] S. Kück, K. Petermann, U. Pohlmann, and G. Huber, Electronic and vibronic transitions of the Cr^{4+}-Doped Garnets $Lu_3Al_5O_{12}$, $Y_3Al_5O_{12}$, $Y_3Ga_5O_{12}$ and $Gd_3Ga_5O_{12}$, J. Lumin. **68**, 1 (1996).

[51] M. Back, J. Ueda, H. Nambu, M. Fujita, A. Yamamoto, H. Yoshida, H. Tanaka, M. G. Brik, and S. Tanabe, Boltzmann thermometry in Cr^{3+}-doped Ga_2O_3 polymorphs: The structure matters! Adv. Opt. Mater. **9**, 2100033 (2021).

[52] Y. Xu, Y. Zhang, L. Wang, M. Shi, L. Liu, and Y. Chen, Red emission enhancement for $CaAl_{12}O_{19}:Cr^{3+}$ and $CaAl_{12}O_{19}:Mn^{4+}$ phosphors, J. Mater. Sci. Mater. Electron. **28**, 12032 (2017).

[53] V. Wang, N. Xu, J.-C. Liu, G. Tang, and W.-T. Geng, VASPKIT: A user-friendly interface facilitating high-throughput

computing and analysis using VASP code, Comput. Phys. Commun. **267**, 108033 (2021).

[54] K. Momma and F. Izumi, *VESTA3* for Three-Dimensional visualization of crystal, volumetric and morphology data, J. Appl. Cryst. **44**, 1272 (2011).

[55] L. Martinelli, G. Bevilacqua, and E. E. Vogel, *Optical Properties of 3d-Ions in Crystals: Spectroscopy and Crystal Field Analysis*, edited by N. M. Avram and M. G. Brik (Springer, Berlin, Heidelberg, 2013), pp. 157–202.